

Scalable Aqueous Processing-Based Passive Daytime Radiative Cooling Coatings

Wenlong Huang, Yijun Chen, Yu Luo, Jyotirmoy Mandal, Wenxi Li, Meijie Chen,*
Cheng-Chia Tsai, Zhongqiang Shan, Nanfang Yu, and Yuan Yang*

Passive daytime radiative cooling (PDRC) can realize electricity-free cooling by reflecting sunlight and emitting heat to the cold space. Current PDRC designs often involve costly vacuum processing or a large quantity of harmful organic solvents. Aqueous and paint-like processing is cost-effective and environmentally benign, thereby highly attractive for green manufacturing of PDRC coatings. However, common polymers explored in PDRC are difficult to disperse in water, let alone forming porous structures for efficient cooling. Here, a simple “bottom-up” ball milling approach to create uniform micro-assembly of poly(vinylidene fluoride-co-hexafluoropropene) nanoparticles is reported. The micro- and nanopores among secondary particles and primary particles substantially enhance light scattering and results in excellent PDRC performance. A high solar reflectance of 0.94 and high emittance of 0.97 are achieved, making the coating 3.3 and 1.7 °C cooler than commercial white paints and the ambient temperature, under a high solar flux of $\approx 1100 \text{ W m}^{-2}$. More importantly, the volatile organic compound content in the aqueous paint is only 71 g L^{-1} . This satisfies the general regulatory requirements, which are critical to sustainability and practical applications.

1. Introduction

Cooling is crucial for a wide range of human activities, such as food preservation,^[1] air conditioning,^{[1][2]} and data processing.^[3]

Dr. W. Huang, Dr. Y. Chen, Y. Luo, W. Li, C.-C. Tsai, Prof. N. Yu, Prof. Y. Yang
Program of Materials Science and Engineering
Department of Applied Physics and Applied Mathematics
Columbia University
New York, NY 10027, USA
E-mail: yy2664@columbia.edu

Dr. W. Huang, Prof. Z. Shan
School of Chemical Engineering and Technology
Tianjin University
Tianjin 300350, China

Dr. J. Mandal
Department of Materials Science and Engineering
University of California, Los Angeles
Los Angeles, CA 90095, USA

Prof. M. Chen
School of Energy Science and Engineering
Central South University
Changsha 410083, China
E-mail: chenmeijie@csu.edu.cn

 The ORCID identification number(s) for the author(s) of this article can be found under <https://doi.org/10.1002/adfm.202010334>.

DOI: 10.1002/adfm.202010334

However, the widely used compression-based cooling systems consume a substantial amount of electricity, generate a large quantity of CO_2 , and have a net-heating effect.^{[4],[5]} In contrast, passive daytime radiative cooling (PDRC) with net-cooling capability is energy-saving, environmentally friendly; and thus it has received considerable attentions in recent years.^{[6]–[12]} A PDRC surface typically exhibits high reflectance within the solar spectrum (\bar{R}_{solar} , wavelength $\lambda = 0.3\text{--}2.5 \mu\text{m}$) and high thermal emittance in the atmosphere's long-wave infrared (LWIR) transmission window ($\bar{\epsilon}_{\text{LWIR}}$, $\lambda = 8\text{--}13 \mu\text{m}$). In this case, the energy lost to the cold space by thermal radiation exceeds solar heating even during daytime, and thereby electricity-free and spontaneous subambient cooling is realized.^[13]

Various strategies have been proposed to achieve high-performance PDRC in the past decade,^{[14]–[17]} including flexible coating^{[18],[19]} multilayer photonic structures,^{[6],[20]} inorganic particles/polymer composites film,^{[21]–[23]} and emissive coating on metal substrates,^{[24],[25]} and white cool-roof paints.^{[26]–[29]} Among these, white cool-roof paints remain the most dominant radiative cooling design owing to their low-cost and convenience of application. However, the use of titanium dioxide (TiO_2) pigment to reflect sunlight causes paints to absorb $\lambda < 410 \text{ nm}$ and practically limits their \bar{R}_{solar} to ≈ 0.87 , severely reducing their radiative cooling capability during the day.^[30] To address this issue, recently porous polymers have been demonstrated as an effective method to eliminate absorption by TiO_2 .^{[10],[18],[31]} The abundant nano/micropores inside strongly scatter light in broadband from the ultraviolet to midinfrared spectrum, leading to high \bar{R}_{solar} of 0.96–0.99 and $\bar{\epsilon}_{\text{LWIR}}$ of 0.95–0.97. Such porous coating achieved subambient cooling of $\approx 6 \text{ °C}$ under direct sunlight.^{[10],[18],[31]} Moreover, the excellent stability of fluorinated polymer against ultraviolet light makes it durable for long-term outdoor applications.^{[10],[30]} However, the process to fabricate porous polymer coating often involves a high content of volatile organic compound (VOC) to dissolve polymers (e.g., acetone ($\approx 758 \text{ g L}^{-1}$) for poly(vinylidene fluoride-co-hexafluoropropene)/P(VdF-HFP),^[10] and dimethylformamide ($\approx 750 \text{ g L}^{-1}$) for poly(vinylidene fluoride)/PVdF).^{[32],[33]} Such an amount of VOC not only exceeds enforced environmental standards,^[34] but also increases the production cost. To

realize the fullest applicability and radiative cooling benefit of such super-white coatings, it is necessary and crucial to develop water-based paint coatings with high PDRC performance and low VOC content.

However, two major challenges impede the development of fluorinated polymer-based waterborne coatings with high PDRC performance. First, P(VdF-HFP) and other common fluorinated polymers are highly hydrophobic. They are hardly dispersible and aggregate severely in water (Figure S1 a, Supporting Information). Second, even if primary polymer particles are well dispersed, the as-cast coating only contains nanopores (<100 nm, top row in Figure 1a,b) due to the size restriction of resin particles (≈ 200 nm, Figure S1b–d, Supporting Information), which is much less efficient in light scattering compared to hierarchically micro/nanoporous structure.^[10] In this paper, we developed a surfactant-assisted ball milling strategy to address both challenges together (bottom row in Figure 1a). Unlike conventional thoughts that ball milling breaks or slashes particles, adequate energy input in ball milling enables the self-assembly of P(VdF-HFP) nanoparticles into uniform secondary microparticles (microclusters, 2.0 ± 0.6 μm in diameter), where a high density of micropores and nanopores coexist among secondary and primary particles, respectively. To the best of our knowledge, this ball milling-based strategy has not been reported before. Such a hierarchical structure is efficient in scattering broadband sunlight, leading to high $\bar{R}_{\text{solar}}/\bar{\epsilon}_{\text{LWIR}}$ of 0.94/0.97 at a thickness of 500 μm (Figure 1d; and Figure S2, Supporting Information). Detail measurement can be found in Section 1 of the Supporting Information. More importantly, the VOC content in the formulation decreases to only ≈ 240 g L^{-1} without water, and ≈ 71 g L^{-1} when the mass of the water is also considered (Table S1, Supporting Information), well below the criteria for paints set by the environmental protection agency (EPA) in the United States^[34] (Table S2, Supporting Information). More detail about VOC calculation can be found in Section 2 of the Supporting Information. Such excellent PDRC performance and the scalable, aqueous-based formulation make this strategy sustainable and attractive for practical applications.

2. Results

To address the first challenge of undesirable agglomeration, sodium dodecyl sulfonate (SDS) was added into water as a surfactant to reduce surface tension, thereby promoting the dispersion of P(VdF-HFP) nanoparticles (Figure S1a, Supporting Information). However, with conventional dispersing methods, such as sonication and mechanical stirring, the corresponding P(VdF-HFP) coatings show inevitable cracks (top and middle rows in Figure 1c). Moreover, only mechanical stirring is not enough to break agglomeration; and thus, the as-cast film contains highly inhomogeneous micrometer-sized assemblies of nanoparticles (middle row in Figure 1b), which is ineffective in scattering sunlight. The application of sonication can break agglomeration but the as-cast film only contains uniformly distributed nanoparticles (top row in Figure 1a). The pores among these nanoparticles are much less than 100 nm, which is also inefficient for reflecting sunlight and results in a low \bar{R}_{solar} .

The inefficiency of these two structures is proved by both numerical full-field electromagnetic simulations of 20 μm thick films and optical measurements of 200 μm thick films (Figures S3 and S4, Supporting Information). 20 μm is chosen due to considerations on computational cost, and 200 μm is selected as thicker nanoparticles and nonuniform microclusters-based films show inevitable cracks, which impedes accurate optical measurements. The nanoparticle-based films display low \bar{R}_{solar} of 0.37 in simulation and 0.80 in optical measurements, and the nonuniform microcluster-based films show low \bar{R}_{solar} of 0.37 in simulation and 0.84 in optical measurements. In contrast, when a film with uniform micrometer-sized secondary particles (bottom row in Figure 1a,b) is considered as a potential possibility, the hierarchically porous structure formed by both micropores among microclusters and nanopores among primary particles leads to a higher \bar{R}_{solar} of 0.43 in simulation, and 0.87 in experiments.

To obtain this favorable structure for PDRC and thus address the second challenge, we developed a simple ball milling strategy to assemble P(VdF-HFP) nanoparticles into the desired uniform microclusters shown in the bottom row of Figure 1a. This approach appears counterintuitive since ball milling is conventionally used to squash bulk materials or break down agglomerates.^{[35]–[37]} However, we find that ball milling with appropriate energy input only causes slight plastic deformation of primary P(VdF-HFP) nanoparticles, which is beneficial for them to form microclusters with relatively uniform sizes (Figure 2). At low speed (e.g., <200 rpm, stage I), the energy input only triggers the elastic deformation of nanoparticles (Figure 2a). With the assistance of surfactant, large P(VdF-HFP) agglomerates are dispersed, forming a nanoparticle-dominated coating. However, nanopores inside (<100 nm) fail to reflect sunlight efficiently, and the corresponding \bar{R}_{solar} is only 0.91 (Figure S5 a,b, Supporting Information). Upon increasing milling speed, more energy is continuously transferred to P(VdF-HFP) nanoparticles and gradually induces plastic deformation (Figure 2b). At a moderate speed (e.g., 285 rpm, stage II), the energy is high enough to not only disassemble P(VdF-HFP) nanoparticles in their original agglomerates but also initiate plastic deformation of polymer particles, which promotes the dispersed nanoparticles to bind together and “assemble” into microclusters (Figure 2b). Hence, the rich hierarchical micro/nanopores inside lead to an optimal \bar{R}_{solar} of 0.94 (Figure 1d; and Figure S5b, Supporting Information), together with a high $\bar{\epsilon}_{\text{LWIR}}$ of 0.96. Moreover, due to the randomized and anisotropic pore orientation, \bar{R}_{solar} and $\bar{\epsilon}_{\text{LWIR}}$ also show weak angular dependence. \bar{R}_{solar} remains at 0.94 at 50° and 70°, respectively, and $\bar{\epsilon}_{\text{LWIR}}$ stays as high as 0.95 and 0.92 at 50° and 70°, respectively (Figure 1e,f).

On the other side, excessive energy will bring about severe plastic deformation and lead to the formation of cold-welding-like plates. For instance, when the milling speed is increased to 380 rpm (stage III), the boundaries between P(VdF-HFP) nanoparticles disappear completely (Figure 2c). The densified plates reduce the porosity of the P(VdF-HFP) coating (Table S3, Supporting Information), which is unfavorable for reflecting sunlight, and \bar{R}_{solar} is reduced to only 0.90 (Figure S5, Supporting Information). In addition to milling speed, the ball milling time has a similar effect on the morphological evolution

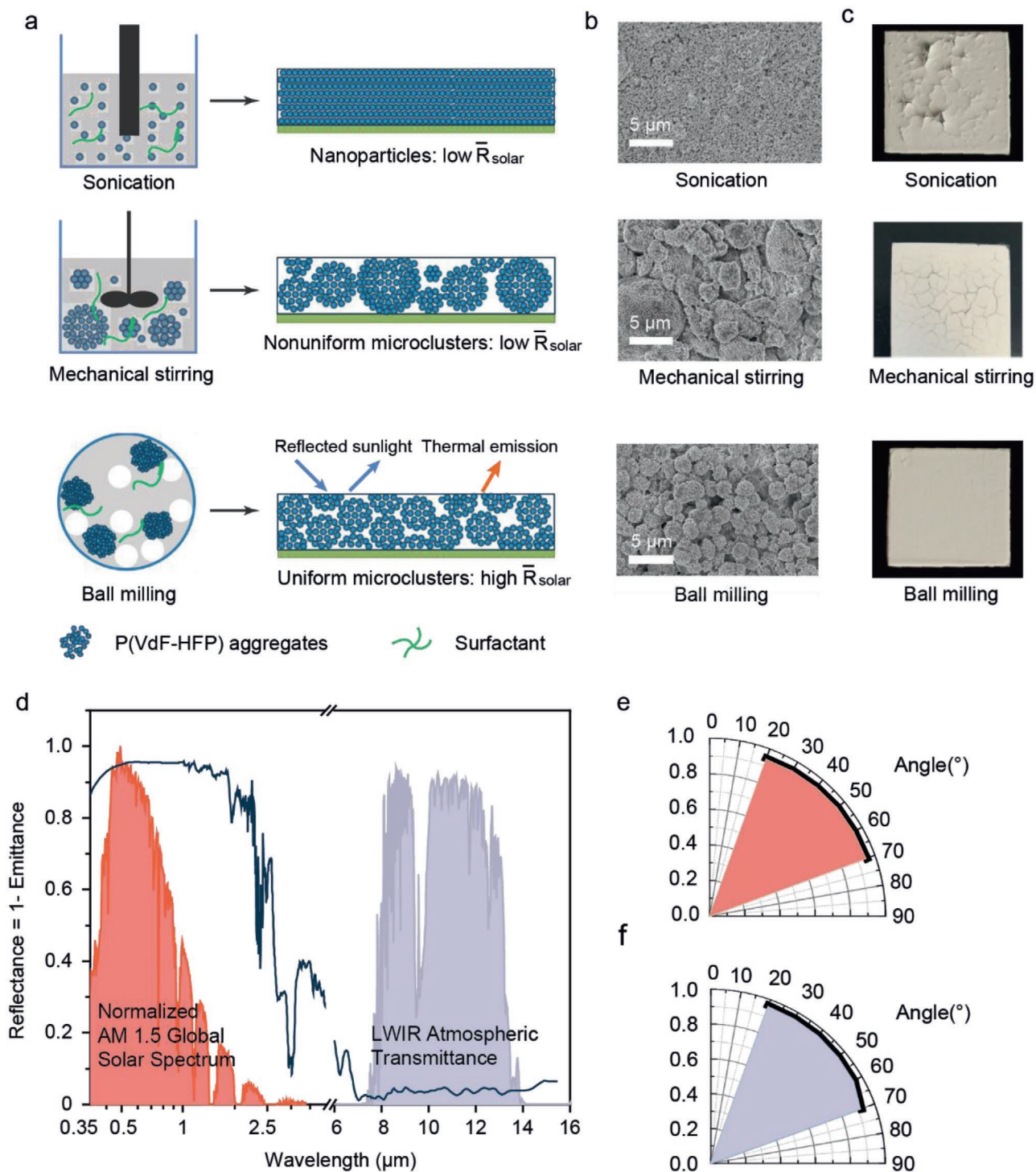


Figure 1. The design principle of aqueous processing-based porous P(VdF-HFP) coatings. a) The schematic illustrations, b) SEM images, and c) optical images of aqueous processing-based P(VdF-HFP) coatings with different dispersing methods, which render various morphologies. Top row: sonication (nanoparticles-based film). Middle row: mechanical stirring (nonuniform microclusters-based film). Bottom row: ball milling with adequate energy input (uniform microclusters-based film). In c), the top and middle ones are 250 μm thick and the bottom one is 800 μm thick. This is to show that there is no crack even in thick films by the ball milling strategy. d) The spectral reflectance ($R = 1 - \epsilon$) of a 500 μm thick porous P(VdF-HFP) coating prepared by the ball milling approach in a). The wavelength range in d) is 0.35–5.0 μm and 6.0–15.4 μm . The data are presented against normalized ASTM G173 Global solar spectrum and the LWIR atmospheric transparency window. The organic compound (VOC) content is only 240 g L^{-1} without water included, and 71 g L^{-1} with water included. e) \bar{R}_{solar} and (f) $\bar{\epsilon}_{\text{LWIR}}$ of a porous P(VdF-HFP) coating in d) at different incident angles, which was prepared by the ball milling approach.

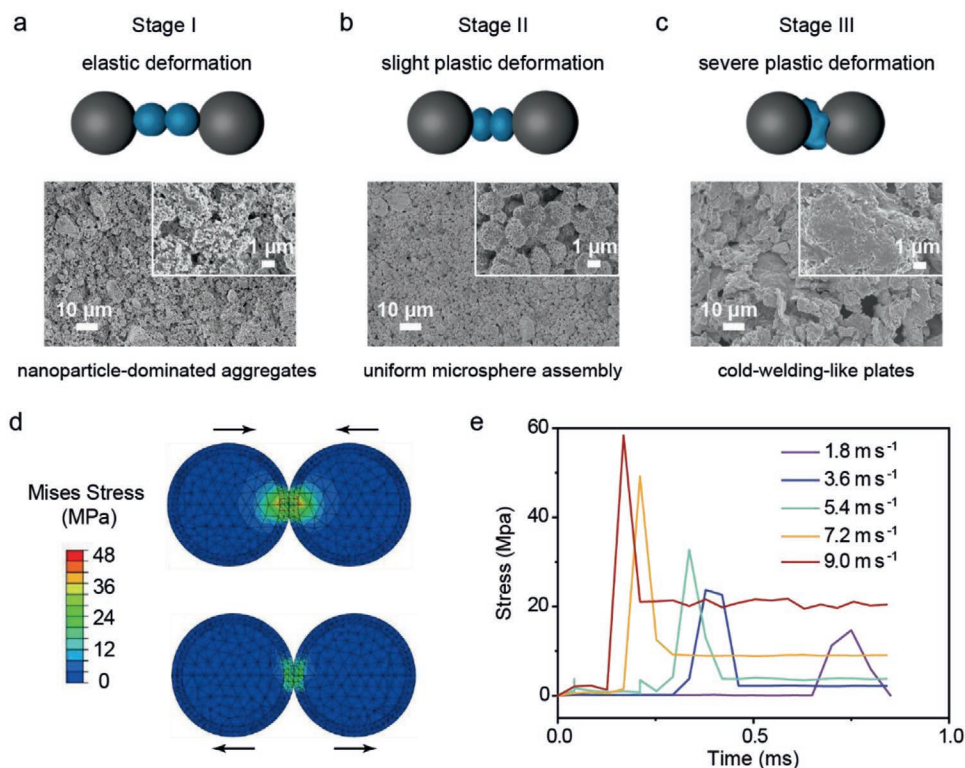


Figure 2. a) The schematic illustrations of different mechanical deformation stages in ball milling: stage I: low speed—elastic deformation, stage II: intermediate speed—slight plastic deformation, and stage III: high speed—severe plastic deformation. The bottom row includes corresponding SEM images of P(VdF-HFP) ball-milled at a) stage I – 190 rpm, b) stage II – 285 rpm, and c) stage III – 380 rpm, respectively. The milling time was 2 h for all cases. d) The finite element analysis-based mechanical simulation of the stress distribution of P(VdF-HFP) when the relative speed of two balls is 7.2 m s^{-1} . To simplify the model, P(VdF-HFP) is considered as a coating layer on milling balls with a thickness of $390 \mu\text{m}$. The top figure shows the moment that two balls have a relative speed of zero, and the bottom is during bouncing back. e) The temporal evolution of stress at the cross point of the line connecting two ball centers and the ZrO_2 /polymer interface during the collision at different relative velocities. This position bears the largest stress in the collision process.

of P(VdF-HFP). Taking the milling speed of 285 rpm as an example, either too short or too long time cannot form well-assembled microclusters suitable for PDRC (Figures S5 and S6, Supporting Information). Further optical measurements show that the optimal ball milling time should be 2 h at 285 rpm, which give the highest \bar{R}_{solar} of 0.94 shown in Figure 1d.

Such experimental observations on the optimal milling speed and time for slight plastic deformation is also echoed by finite element analysis-based mechanical simulations. In the simulation, we assume that two ZrO_2 balls with diameters of 5 mm move towards each other (Figure 2d) and each ball is covered by a P(VdF-HFP) film with a thickness of $390 \mu\text{m}$ based on the concentration of P(VdF-HFP) in the milling slurry. Moreover, the relative speed of balls is estimated to be in the range of $1.8\text{--}9.0 \text{ m s}^{-1}$ based on the rotation speed and the miller geometry. Details of these assumptions and estimations can be found in Section 3 of the Supporting Information (Table S4, Supporting Information). Given this, we simulate the collision process of two balls and estimate the maximum stresses during the collision at relative speeds of 1.8, 3.6, 5.4, 7.2, and 9.0 m s^{-1} , respectively. The simulation shows that the maximum Mises stress on P(VdF-HFP) particles occurs when two balls are closest to each other (Figure 2d). The maximum stress at 1.8, 3.6, 5.4, 7.2, and 9.0 m s^{-1} reaches 15, 24, 33, 48, and 58 MPa (Figure 2e),

respectively, which are similar to the yield strength of 42 MPa for P(VdF-HFP).^[38] The results support that ball milling at 285 rpm not only breaks undesired agglomeration among P(VdF-HFP) particles but also induces a slight degree of plastic deformation with a high probability. Such an adequate degree of deformation facilitates the assemble of microclusters without destroying nanopores among primary nanoparticles substantially, and the as-formed hierarchically porous structure benefits PDRC performance significantly, as discussed above.

The ball-milled slurry shows both excellent storage stability and processability to form uniform coatings. First, with the addition of sodium carboxymethyl cellulose (CMCNa) as the thickening agent, and styrene-butadiene rubber (SBR) emulsion as the binder, no sedimentation was observed for the slurry even after being stored still for 2 months (Figure 3a). Second, to form coatings, the well-dispersed slurry is cast onto a substrate, followed by doctor-blade application and drying process illustrated in Figure S7 (Supporting Information). The coating from the ball-milled slurry shows no cracks at $800 \mu\text{m}$ in thickness, while obvious cracks exist in those derived from sonication and mechanical stirring, even at $250 \mu\text{m}$ in thickness (Figure 1c). Such better processability can be attributed to slight plastic deformation in ball milling, leading to stronger binding between P(VdF-HFP) particles, which suppresses cracks during

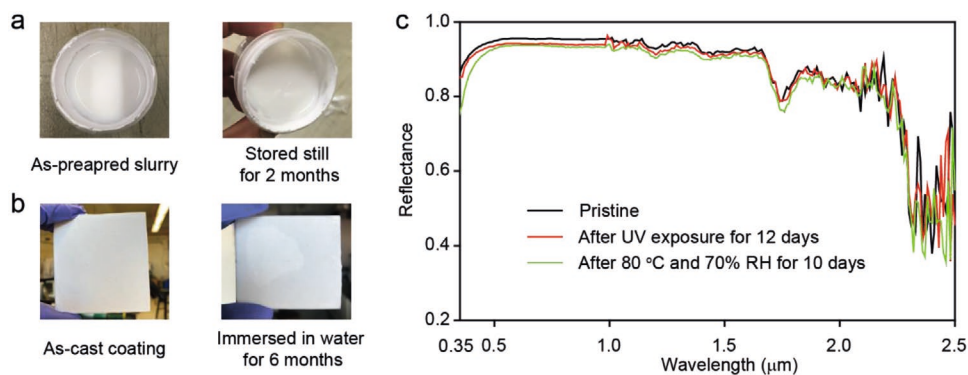


Figure 3. a) The storage stability of the ball-milled P(VdF-HFP) slurry. Left: as-prepared slurry. Right: the slurry after being stored for 2 months. b) The stability of an aqueous process-based P(VdF-HFP) coating in water. Left: an as-prepared coating. Right: the coating after being immersed in water for 6 months. c) The reflectance spectra of a 500 μm thick P(VdF-HFP) coating in the pristine state (black), after UV exposure for 12 days (red), and after aging at 80 °C and 70% relative humidity for 10 days (green). The wavelength range in c) is 0.35–2.5 μm.

the subsequent drying step. In all slurries, we also added 0.5 wt% of commercial topcoat and 0.75 wt% of acrylate oligomer (polyethylene glycol dimethacrylate, PEGDMA) as a hardener and a UV crosslinker, respectively, which helps further enhance the coating's adhesion to substrates. As shown in the peeling-off tests, these two additives enhance the peeling strength from 1.2 to 3.1 N m⁻¹ on an Al substrate (Figure S8, Supporting Information). Besides Al, this coating can be easily applied to various substrates including PMMA, Cu foil, and wood (Figure S9, Supporting Information). It should be noted that all data reported in this work are based on samples with topcoat and PEGDMA unless specified.

In addition to good processability, the P(VdF-HFP) coating also exhibits excellent stabilities against water and outdoor environments. As shown in Figure 3b, there are no cracks or peeling on the coating even after being immersed in water for 6 months. Such good water-proof capability originates from the hydrophobicity of P(VdF-HFP)^[39] and SBR.^[40] When exposed outdoors for 3 months, the coating appears the same as the pristine state without any cracks (Figure S10, Supporting Information). During accelerated aging tests, the P(VdF-HFP) coating also displays good resistance to UV radiation and thermal

degradation (Figure 3c). For instance, \bar{R}_{solar} of a P(VdF-HFP) coating decreases only slightly from 0.939 to 0.928 even after a 288 h UV exposure (wavelength 395–400 nm) at 135 W m⁻², which is equivalent to half a year of outdoor exposure in the New York City. Moreover, after an as-cast P(VdF-HFP) coating was placed in a chamber at 80 °C and 70% relative humidity for 10 days, its \bar{R}_{solar} only decreases slightly from 0.939 to 0.920.

To investigate the PDRC performance of aqueous paints developed above, field tests were carried out in Los Angeles, CA. The setup is shown in Figure 4a with thermocouple well shielded by both white paper and aluminum foil, and under good ventilation (Figure S11, Supporting Information).^[41] More simulation detail can be found in Section 3 of the Supporting Information (Table S4, Supporting Information). Commercial TiO₂-based paint was used as a control sample, which has $\bar{R}_{\text{solar}}/\bar{\epsilon}_{\text{LWIR}}$ of 0.87/0.93 (Figure S12, Supporting Information). Under a peak solar intensity (I_{solar}) of ≈1100 W m⁻², the P(VdF-HFP) coating without any convection shield has an average surface temperature of ≈30.2 °C, which is averagely 1.7 °C lower than the ambient temperature, and ≈3.3 °C lower than the TiO₂ control (Figure 4b). The excellent PDRC capability is superior to commercial TiO₂ paints and highlights the importance of

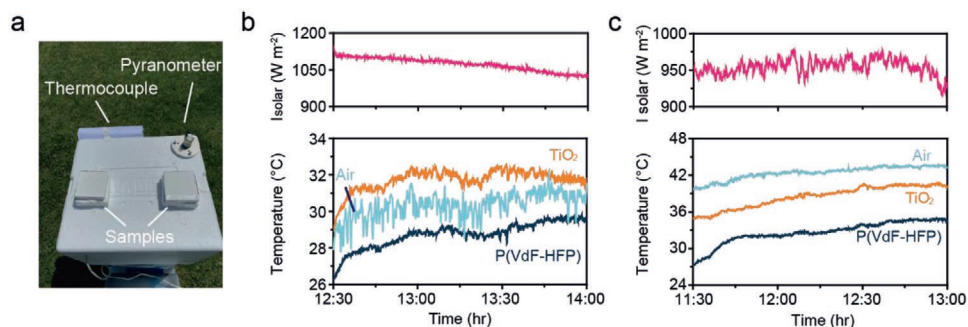


Figure 4. a) A photograph of the setup for testing radiative cooling performance under sunlight. b/c) The real-time data of solar intensity (I_{solar}) and recorded temperatures b) without and c) with a polyethylene cover. The commercial TiO₂ paint and the porous P(VdF-HFP) coating have thicknesses of ≈250 and ≈500 μm, respectively, to ensure the same solid loading (≈0.039 g cm⁻² for the commercial TiO₂ paint and 0.040 g cm⁻² for the porous P(VdF-HFP) coating, respectively). The 250 μm thick TiO₂ coating has nearly identical reflectance spectra as 500 μm thick TiO₂ coating, so that its thickness does not affect comparison results. Detailed analysis can be found in Section 4 of the Supporting Information. Locations and weather: Los Angeles Elevation 212 m, b) Date: 2020-05-25, Air temperature ≈32 °C, wind Speed: 20 km h⁻¹, and c) Date: 2020-04-14, Air temperature outside the box ≈26 °C based on the local weather station, wind speed: 9 km h⁻¹.

creating hierarchically porous structures by ball milling with rationally tuned energy input. In another experiment to minimize the effects of air convection, both aqueous P(VdF-HFP) paint and TiO₂-based paint control were tested with a polyethylene film cover (Figure S11b, Supporting Information). Under a solar flux of $\approx 950 \text{ W m}^{-2}$, the P(VdF-HFP) coating's temperature is $\approx 9.5 \text{ }^\circ\text{C}$ cooler than the air inside the chamber, and $\approx 6.2 \text{ }^\circ\text{C}$ cooler than the TiO₂ paint (Figure 4c), further demonstrating the better cooling capability of as-cast aqueous P(VdF-HFP) paint. In addition, the reliability of the setup in Figure 4a has been validated by COMSOL simulation (Figure S11, Supporting Information).

3. Conclusions

In this work, we have successfully realized an aqueous processing-based P(VdF-HFP) coating with both excellent PDRC performance and low VOC content. A simple and innovative “bottom-up” ball milling approach was developed. By tuning energy input in ball milling, slight plastic deformation of primary P(VdF-HFP) nanoparticles was induced, which leads to the assembly of nanoparticles into uniform microclusters with favorable particle size. The hierarchically porous structure formed by stacking among secondary particles and primary particles is efficient to scatter sunlight and eventually leads to excellent PDRC performance ($\bar{R}_{\text{solar}} = 0.94$ and $\bar{\epsilon}_{\text{LWIR}} = 0.97$), which are also validated by theoretical simulation and comparative experiments. The VOC content is reduced down to 240 g L^{-1} without water or 71 g L^{-1} with water counted, which addresses a major challenge in previous organic solvent-based processing for PDRC paints.^{[10],[41]} Moreover, the excellent storage stability, water-proof, and antiaging capability of the as-developed P(VdF-HFP) coating also make this strategy feasible for large-scale applications in PDRC. Our work provides a guide for designing environmental benign, water-based P(VdF-HFP) coating in PDRC, which can be further extended to other polymers such as poly(vinylidene fluoride) (PVdF) and polytetrafluoroethylene (PTFE).

4. Experimental Section

Preparation of Aqueous P(VdF-HFP) Coating: Three different methods including ball milling, mechanical stirring, and sonication were explored for preparing water-based P(VdF-HFP) slurries. For the ball milling process, 3 g of P(VdF-HFP) resin (Kynar Flex 2801), 30 mg of sodium dodecyl sulfate (SDS) and 7.5 g of water were added into a 50 mL ball milling jar together with 48 g of zirconia beads (diameter of 5 mm) as the milling media. For mechanical stirring, the same ingredients above were dispersed via a stirring bar (length of 1.5 cm in a 20 mL vial) driven by a conventional mini-stirrer (IKA Magnetic stirrers, topolino) at a speed of $\approx 900 \text{ rpm}$ for 12 h. For the sonication treatment, the same mixture was subjected to sonication for 12 h with mechanically stirring of 15 min every 2 h. In addition, in the sonication method only, extra surfactants of OP-10 (30 mg) and triethyl phosphate (300 mg) were added into the mixture to realize better dispersion.

Once the dispersing process was completed, 750 mg of isopropyl alcohol was added to eliminate bubbles produced, followed by adding 30 mg of sodium carboxymethyl cellulose (CMCNa) for thickening the slurries. Next, 300 mg of styrene butadiene rubber emulsion was added to the slurries above as the binder. To enhance the mechanical strength

of the subsequent coating, 30 mg of photopolymerizable polyethylene glycol dimethacrylate (PEGDMA, 30 mg) and photoinitiator irgacure 1173 (0.3 mg) were further introduced into the slurries. These additives were added to samples dispersed by all three methods. After being homogenized, the P(VdF-HFP) paste was blade-coated on poly (methyl methacrylate) plate and then UV-cured for 5 min so as to promote the crosslinkage, followed by drying for 10 min. The power of the UV light (QUANS, UV LED Flood Light, $\lambda = 395\text{--}400 \text{ nm}$) intensity is 135 W m^{-2} .

Optical Characterizations: For the ultraviolet range (0.35–0.4 μm), measurement was taken using a UV spectrophotometer (Lambda 950, PerkinElmer) equipped with Tungsten–Halogen and Deuterium Lamps as light sources, a photomultiplier tube and PbS sensor as detectors, and an integrating sphere module with a 15 cm sphere and standard Spectralon-SRM 99 references. For the visible and near-infrared range (0.4–1.1 μm), the spectra were measured by a Si photodiode with a monochromatic incident beam, generated by a supercontinuum laser and a wavelength-tunable monochromator. An integrating sphere with a silicon detector (Model IS200, Thorlabs) was used in combination with a high-power continuous laser emitter (SuperK Extheme, Photonics) and a tunable filter (Fianium LLTF contrast) to measure the reflectance. The sample was placed inside an integrating sphere, using a calibrated diffuse reflector (Item SM05CP2C) as a reference. For the near-to-mid-infrared band (1.1–15.4 μm), the spectra were measured by a Fourier transform infrared spectroscope with thermal sources and a Mercury-Cadmium-Telluride detector. The reflectance was measured using a gold integrating sphere (Model 4P-GPS-020-SL, Labsphere), a mercury cadmium telluride detector, and a Fourier transform infrared spectrometer (Vertex 70v, Bruker). A gold-plated aluminum foil was used as a reference.

Field Tests: The device for field tests is shown in Figure 4a. A water-based porous P(VdF-HFP) coating and a TiO₂ slab coating were placed in a transparent polycarbonate box with the top open. In the case with cover, a low-density transparent polyethylene film was used to cover the box to minimize heat exchange caused by air convection, while not affecting solar and infrared transparency significantly. All samples were cushioned with polystyrene foam. To monitor sample temperatures, thermocouples were pressed against the back of the samples with black tapes as a solar absorption layer. As a comparison, a blank thermocouple was placed in a shaded place in the box to measure the air temperature. The configuration is the same as Figure S11a Supporting Information). In order to measure the total solar intensity (including direct and diffuse reflection), a pyranometer (Apogee, SP510) was placed next to the sample and connected to a computer.

More details of the Experimental Section can be found in the Supporting Information.

Supporting Information

Supporting Information is available from the Wiley Online Library or from the author.

Acknowledgements

W.H., Y.C., Y.L., and J.M. contributed equally to this work. Y.Y. acknowledges support from the National Science Foundation (Award No. 2005747). W.H. would like to acknowledge the financial support from the China Scholarship Council (No. 201806250099). J.M. was supported by Schmidt Science Fellows, in partnership with the Rhodes Trust. The authors would like to thank Prof. Aaswath Raman for use of their spectrophotometer to take ultraviolet reflectance measurements.

Conflict of Interest

The authors declare no conflict of interest.

Data Availability Statement

Research data are not shared.

Keywords

aqueous processing, ball milling, fluoropolymer, green manufacturing, passive daytime radiative cooling

Received: December 1, 2020

Revised: February 13, 2021

Published online:

-
- [1] Z. Zhu, Y. Geng, D. W. Sun, *Trends Food Sci. Technol.* **2019**, *85*, 67.
- [2] F. Meggers, H. Guo, E. Teitelbaum, G. Aschwanden, J. Read, N. Houchois, J. Pantelic, E. Calabrò, *Energy Build.* **2017**, *157*, 11.
- [3] R. Lent, *Future Gener. Comput. Syst.* **2016**, *57*, 1.
- [4] <https://data.worldbank.org/indicator/EG.ELC.ACCS.RU.ZS> (accessed: February 2020)
- [5] <https://www.epa.gov/ods-phaseout> (accessed: February 2020)
- [6] A. P. Raman, M. A. Anoma, L. Zhu, E. Rephaeli, S. Fan, *Nature* **2014**, *515*, 540.
- [7] T. Li, Y. Zhai, S. He, W. Gan, Z. Wei, M. Heidarinejad, D. Dalgo, R. Mi, X. Zhao, J. Song, J. Dai, C. Chen, A. Aili, A. Vellore, A. Martini, R. Yang, J. Srebric, X. Yin, L. Hu, *Science* **2019**, *364*, 760.
- [8] N. N. Shi, C. C. Tsai, F. Camino, G. D. Bernard, N. Yu, R. Wehner, *Science* **2015**, *349*, 298.
- [9] Y. Zhai, Y. Ma, S. N. David, D. Zhao, R. Lou, G. Tan, R. Yang, X. Yin, *Science* **2017**, *355*, 1062.
- [10] J. Mandal, Y. Fu, A. C. Overvig, M. Jia, K. Sun, N. N. Shi, H. Zhou, X. Xiao, N. Yu, Y. Yang, *Science* **2018**, *362*, 315.
- [11] A. Leroy, B. Bhatia, C. C. Kelsall, A. Castillejo-Cuberos, M. H. Di Capua, L. Zhao, L. Zhang, A. M. Guzman, E. N. Wang, *Sci. Adv.* **2019**, *5*, eaat9480.
- [12] X. Yin, R. Yang, G. Tan, S. Fan, *Science* **2020**, *370*, 786.
- [13] D. Li, X. Liu, W. Li, Z. Lin, B. Zhu, Z. Li, J. Li, B. Li, S. Fan, J. Xie, J. Zhu, *Nat. Nanotechnol.* **2021**, *16*, 153.
- [14] Y. Yang, Y. Zhang, *MRS Energy Sustainable* **2020**, *7*, E18.
- [15] B. Zhao, M. Hu, X. Ao, N. Chen, G. Pei, *Appl. Energy* **2019**, *236*, 489.
- [16] Z. Chen, L. Zhu, A. Raman, S. Fan, *Nat. Commun.* **2016**, *7*, 13729.
- [17] X. Xue, M. Qiu, Y. Li, Q. M. Zhang, S. Li, Z. Yang, C. Feng, W. Zhang, J. G. Dai, D. Lei, W. Jin, L. Xu, T. Zhang, J. Qin, H. Wang, S. Fan, *Adv. Mater.* **2020**, *32*, 1906751.
- [18] X. Wang, X. Liu, Z. Li, H. Zhang, Z. Yang, H. Zhou, T. Fan, *Adv. Funct. Mater.* **2020**, *30*, 1907562.
- [19] H. Zhang, K. C. S. Ly, X. Liu, Z. Chen, M. Yan, Z. Wu, X. Wang, Y. Zheng, H. Zhou, T. Fan, *Proc. Natl. Acad. Sci. USA* **2020**, *117*, 14657.
- [20] W. Li, S. Fan, *Opt. Express* **2018**, *26*, 15995.
- [21] A. W. Harrison, M. R. Walton, *Sol. Energy* **1978**, *20*, 185.
- [22] A. R. Gentle, G. B. Smith, *Nano Lett.* **2010**, *10*, 373.
- [23] S. Atigyanun, J. B. Plumley, S. J. Han, K. Hsu, J. Cytrynbaum, T. L. Peng, S. M. Han, S. E. Han, *ACS Photonics* **2018**, *5*, 1181.
- [24] L. Zhou, H. Song, J. Liang, M. Singer, M. Zhou, E. Stegenburgs, N. Zhang, C. Xu, T. Ng, Z. Yu, B. Ooi, Q. Gan, *Nat. Sustainability* **2019**, *2*, 718.
- [25] C. G. Granqvist, A. Hjortsberg, *J. Appl. Phys.* **1981**, *52*, 4205.
- [26] B. Orel, M. K. Gunde, A. Krainer, *Sol. Energy* **1993**, *50*, 477.
- [27] P. Berdahl, S. E. Bretz, *Energy Build.* **1997**, *25*, 149.
- [28] R. Levinson, H. Akbari, *Energy Effic.* **2010**, *3*, 53.
- [29] J. Song, J. Qin, J. Qu, Z. Song, W. Zhang, X. Xue, Y. Shi, T. Zhang, W. Ji, R. Zhang, H. Zhang, Z. Zhang, X. Wu, *Sol. Energy Mater. Sol. Cells* **2014**, *130*, 42.
- [30] J. Mandal, Y. Yang, N. Yu, A. P. Raman, *Joule* **2020**, *4*, 1350.
- [31] J. Mandal, M. Jia, A. Overvig, Y. Fu, E. Che, N. Yu, Y. Yang, *Joule* **2019**, *3*, 3088.
- [32] M. mi Tao, F. Liu, B. rong Ma, L. xin Xue, *Desalination* **2013**, *316*, 137.
- [33] I. N. Bhatti, *IOSR J. Appl. Phys.* **2013**, *4*, 42.
- [34] <https://www.govinfo.gov/content/pkg/CFR-2016-title40-vol6/pdf/CFR-2016-title40-vol6-part59.pdf> (accessed: March 2020)
- [35] P. Baláž, M. Achimovicová, M. Baláž, P. Billik, C. Z. Zara, J. M. Criado, F. Delogu, E. Dutková, E. Gaffet, F. J. Gotor, R. Kumar, I. Mitov, T. Rojac, M. Senna, A. Streletskii, W. C. Krystyna, *Chem. Soc. Rev.* **2013**, *42*, 7571.
- [36] H. S. Kim, B. Madavali, T. J. Eom, C. M. Kim, J. M. Koo, T. H. Lee, S. J. Hong, *Arch. Metall. Mater.* **2015**, *60*, 1235.
- [37] F. Delogu, G. Gorrasi, A. Sorrentino, *Prog. Mater. Sci.* **2017**, *86*, 75.
- [38] A. Srivastava, P. Maiti, D. Kumar, O. Parkash, *Compos. Sci. Technol.* **2014**, *93*, 83.
- [39] S. S. Ray, C. K. Deb, H. M. Chang, S. S. Chen, M. Ganesapillai, *J. Appl. Polym. Sci.* **2019**, *136*, 48021.
- [40] A. Sinclair, X. Zhou, S. Tangpong, D. S. Bajwa, M. Quadir, L. Jiang, *ACS Omega* **2019**, *4*, 13189.
- [41] Y. Chen, J. Mandal, W. Li, A. Smith-Washington, C. C. Tsai, W. Huang, S. Shrestha, N. Yu, R. P. S. Han, A. Cao, Y. Yang, *Sci. Adv.* **2020**, *6*, eaaz5413.